H2 production mechanisms in irradiated portlandite: surface and volume contributions

Thibaut Herin, Antonino Alessi, Stéphane Poyet, Pascal Bouniol, Sophie Le Caër

H_2 Production Mechanisms in Irradiated Portlandite: Surface and Volume Contributions

Thibaut Herin[a,b], Antonino Alessi[c], Stéphane Poyet[b], Pascal Bouniol[b] and Sophie Le Caër[a*]

[a] *Université Paris-Saclay, CEA, Service de recherche en Corrosion et Comportement des Matériaux, 91191 Gif-sur-Yvette, France*

[b] *Université Paris-Saclay, CEA, CNRS, NIMBE UMR 3685, 91191 Gif-sur-Yvette, France*

[c] *LSI, CEA/DRF/IRAMIS, CNRS, Ecole polytechnique, Institut Polytechnique de Paris, Route de Saclay, F-91128 Palaiseau, France*

* *email: sophie.le-caer@cea.fr*

Abstract

Calcium hydroxide or portlandite ($Ca(OH)_2$) is the second most abundant hydrate in cementitious materials. The latter form the basis of the coating matrices of some forms of radioactive waste. Under ionizing radiation, this results in the production of radiolytic molecular hydrogen, which, when it accumulates in the environment, may raise safety concerns. It is important, therefore, to understand how radiation interacts with these materials, and especially with portlandite. This hydroxide is of particular interest: on exposure to irradiation, it not only leads to the immediate production of molecular hydrogen but also to a delayed production over long periods of time (days or even weeks) after the irradiation stops. It follows that it is important to determine the reaction mechanisms operating in this system. This was carried out here based on experiments with electron paramagnetic resonance spectroscopy, which identified the different radicals generated under radiation. As a result, we have been able to show that the immediate production of H_2 is due to the stabilization of electrons on the surface of the portlandite, followed by surface reactions that encourage the immediate release of H_2 into the gaseous atmosphere. When the dose increases, the number of these sites drops, leading to a fall in the production of the molecular hydrogen immediately released. The delayed production of H_2 is due to the formation of hydrogen atoms followed by their dimerization within the portlandite crystal lattice, with the result that the molecular hydrogen molecules are trapped. In this case, the movement of the hydrogen atoms in the crystal lattice sets the $CaO^{\bullet}$ radicals in motion. At low doses, these radicals dimerize to form $CaO\text{-}OCa$ peroxides. At higher doses, the $CaO^{\bullet}$ radicals can react with hydrogen atoms, which restricts the formation of the trapped H_2. The range of different reaction intermediates identified reflects the richness of the

chemical processes involved in the mechanisms, which accounts for the behavior of portlandite on exposure to irradiation.

Keywords

Portlandite; H_2 production; ionizing radiation; electron paramagnetic resonance (EPR); reaction mechanisms

Introduction

Some types of radioactive waste (Low- and Intermediate-Level radioactive Waste, L&ILW) are conditioned by means of coating matrices made from cementitious materials.[1–3] When exposed to ionizing radiation generated by radioactive waste, these matrices lead to the production of H_2 via O-H group radiolysis. Calcium hydroxide or portlandite ($Ca(OH)_2$; see the compound's structure in Figure 1) is the second most abundant hydrate present in cementitious materials.[4,5] Accordingly, it is a significant reservoir of O-H bonds (3.64×10^{22} cm^{-3}) that may make a substantial contribution to the production of H_2 by the solid phase. We should point out here that the accumulation of H_2 in the atmosphere/environment may pose a risk of explosion/detonation if the content is above the value of 4 vol%.

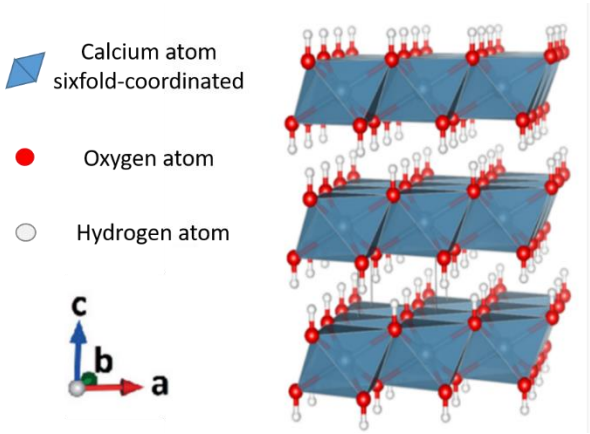

Fig. 1. *Structure of portlandite $Ca(OH)_2$ (illustration created using Vesta software [6]).*

Several studies have shown that exposing portlandite samples to ionizing radiation results in the production of H_2.[2,7,8] The H_2 radiolytic yield values available in the literature are relatively variable, ranging from 0.3×10^{-8} $mol.J^{-1}$ [8] to 2.1×10^{-8} $mol.J^{-1}$ [7]. We recently demonstrated that certain factors - the specific surface area, for example, or the dose rate or presence of adsorbed water on the surface of the mineral - have a significant effect on H_2 production. This makes it difficult to compare different studies with one another.[8] In addition, we also showed that a

portion of the H_2 created during irradiation remains stored in the material. It is subsequently released in a gradual process over several days/weeks (known as "delayed H_2")[8] since this molecule diffuses very slowly within the crystal lattice. By contrast, the H_2 measured directly after irradiation is called "immediate H_2". In addition, the proportion between the molecular hydrogen measured immediately after irradiation and the molecular hydrogen gradually released by the material depends on the size of the portlandite particles and, accordingly, the material's specific surface area. However, the different mechanisms for explaining this production of H_2, and the immediate and delayed production in particular, are still relatively unclear, and the intermediate species involved in the formation processes are still not known. To gain insight into these mechanisms, electron paramagnetic resonance (EPR) is the preferred technique; this can be used to observe and identify the radical species formed. Although numerous studies have been dedicated to the EPR analysis of metal oxides,[9–12] the same is not true for hydroxides. Nevertheless, earlier work focused on the formation of radicals created after gamma irradiation in portlandite.[13–15] This study, however, has concentrated on identifying species rather than determining reaction mechanisms. Consequently, we used EPR with the aim of: (i) identifying the radical species formed during the irradiation of portlandite samples; (ii) determining the reaction mechanisms that explain the production of radiolytic H_2; and (iii) understanding the recycling mechanisms that explain the decreased production of molecular hydrogen from portlandite when the irradiation dose increases.

Materials and methods

$Ca(OH)_2$ synthesis. Several $Ca(OH)_2$ powders were made. All the syntheses were performed in a glove box under a nitrogen flow to protect the $Ca(OH)_2$ from carbonation. The most used $Ca(OH)_2$ powder was prepared by adding 150 mL of ultra-pure water (18.2 MΩ.cm) to the CaO powder (Sigma Aldrich, 99.998%). The resulting mixture was immediately stirred by hand for 2 minutes before being filtered using a Buchner funnel with a fritted glass of porosity 4. The resulting $Ca(OH)_2$ powder was dried under nitrogen for 2 days. This powder is called $Ca(OH)_2$ U.P. (ultra-pure) owing to the purity of the CaO precursor used.

The U.P. portlandite powder was transferred to a hydrothermal reactor and placed in a furnace in order to obtain another powder with a similar composition but with a lower specific surface area. The device was first heated to 373 K for 1 hour; the temperature was then increased to 513 K at a rate of 2 $K.min^{-1}$. The sample was maintained at 513 K for 1 hour; the temperature was then reduced to 373 K at a rate of -2 $K.min^{-1}$ and maintained at the same value for 1 hour.

This process was repeated a total of 8 times. The resulting recrystallized portlandite is called $Ca(OH)_2$ U.P.-L.S. (Ultra-Pure-Low Surface).

To study the impact of the purity of the powder, a third powder was prepared using the same protocol as the U.P. portlandite, but with a CaO powder (Sigma Aldrich, 99.95%) of slightly lower purity as base material. This powder is called L.P. (low purity) portlandite. L.P. portlandite powder is the same as the H.S. portlandite used in our previous study.[8]

Characterization. The portlandite powders were characterized by X-ray diffraction (**Fig. S1 in Supporting Information**). The thermogravimetric analysis of the powders (**Fig. S2 in Supporting Information**) showed that all the portlandites studied had a molar content of calcite of between 1% and 2% (corresponding to the fraction of calcium atoms engaged in a $CaCO_3$ pattern).

We demonstrated that manganese in the form of Mn^{2+} complicates the interpretation of EPR spectra to a significant degree, even if it is present in very low quantities. Quantitative analyzes were performed by ICP-MS (inductively coupled plasma mass spectrometry) in order to estimate its concentration. Approximately 30 mg of $Ca(OH)_2$ powder was diluted in 10 mL of ultrapure water containing 4% by mass of nitric acid. A calibration curve, recorded on control solutions containing between 1 $\mu g.L^{-1}$ and 90 $\mu g.L^{-1}$ of manganese were used to assess the manganese content of the different $Ca(OH)_2$ powders (**see Table 1**). It goes without saying that the synthesis using the purest precursor reduced the manganese content to a substantial degree.

The nitrogen BET method was used to measure the specific surface area of the powders. Approximately 500 mg of portlandite were introduced into an ampule before being desorbed at 100°C under secondary vacuum for several hours. This step made it possible to degas the samples prior to the specific surface area measurements. The apparatus used for the analyzes was a Micromeritics ASAP 2010. The specific surface area of the U.P. portlandite was approximately 15 $m^2.g^{-1}$. It was around 2 $m^2.g^{-1}$ for the U.P-L.S. portlandite, which illustrates how effective cycling in a hydrothermal reactor is for increasing the size of portlandite particles and reducing the specific surface area of the material. **Table 1** summarizes the characteristics of the various powders that were made.

Table 1. *Properties of the different powders used in this study.*

Type of portlandite	$Ca(OH)_2$ U.P.	$Ca(OH)_2$ U.P.-L.S.	$Ca(OH)_2$ L.P.
Purity of the initial CaO	99.998%	99.998%	99.95%
Specific surface area	15 $m^2.g^{-1}$	2 $m^2.g^{-1}$	25 $m^2.g^{-1}$
Manganese content	< 1 ppm	< 1 ppm	15 ppm

Sample preparation and conditioning. Irradiation and EPR analyzes were conducted by conditioning the $Ca(OH)_2$ powders in NMR tubes (100 MHz) in borosilicate glass 18.3 cm in length with an external diameter of 5 mm and an internal diameter of 4 mm. The tubes were filled with 80 $\pm$10 mg of powder. The mass of powder introduced into each tube was routinely precision-weighed.

When the irradiations were performed in liquid nitrogen, tubes with an external diameter of 4 mm and an internal diameter of 3 mm were employed, and the powder mass was then 50 $\pm$10 mg per tube.

Thermal treatment. A 16-hour thermal treatment at 180°C under primary vacuum was conducted on the powders directly in the tubes in order to remove the water adsorbed on the powders. This treatment was identified as being capable of removing adsorbed water from the surface of the portlandite without damaging the material.[8] During the thermal treatment, the tubes were connected to a vacuum system that brought the total pressure down to 0.1 mbar. The tubes were flame-sealed under vacuum at the end of the treatment. This step meant it was possible to avoid exposing the treated powders to air and the re-adsorption of water.

Irradiation. 10 MeV accelerated electrons (ALIENOR accelerator[16]) were used to irradiate the samples. The dose delivered to the samples was measured via Fricke dosimetry.[17] Given the stopping power of electrons in portlandite and water (ESTAR program[18]), the dose received by the portlandite was deemed to be the same within 10% as the dose received by the water in the Fricke dosimeter. For the irradiation experiments, the dose delivered by the 10 ns pulses of the electron accelerator was 20 Gy (1 Gy = 1 $J \times kg^{-1}$) per pulse with an uncertainty of about 5%. The pulse frequency was restricted to 5 Hz to avoid heating the samples during the irradiation. However, the irradiation of the tubes containing the portlandite powder resulted in radiation-induced defects in the glass as well as blackening it. Nevertheless, the irradiation by accelerated electrons was localized. As a result, defects were only created on one end of the tube. To avoid

superposing the defects in the glass on those in the portlandite powder, the tubes were routinely inverted after irradiation. This made it possible to drop the irradiated powder into the non-irradiated part of the tube. EPR measurements carried out on a test tube that did not contain any powder corroborated the absence of defects in the glass at this location and thus validated this experimental protocol.

Electron paramagnetic resonance measurement (EPR). The EPR spectrometer used was a JEOL JES-X310 with a working frequency of 8.75-9.65 GHz (X band). The modulation frequency was 100 kHz. The spectra were recorded with a modulation amplitude of 0.05 mT for a duration of 8 or 15 minutes. A thermal regulation device was used to adjust the temperature that the analyzes took place at. The accessible temperature range was between -150 and 200°C in practice.

Quantification of EPR defects. EPR is a quantitative method.[19] It was possible to estimate the concentration of radiation-induced paramagnetic defects by mass unit in the sample (C_{spin} in **Eq. 3**). To perform that, the normalized double integral of the EPR signals (I_{norm} in **Eq. 1**) is compared to the normalized double integral derived from control samples containing a known quantity of spins (N_{ref} in **Eq. 2**). This made it possible to estimate the absolute quantity of spin (N_{spin} in **Eq. 2)** contained in the studied sample. The concentration of spin C_{spin} is then obtained by dividing the result by the mass of the sample (**Eq. 3**). In theory, the intensity of the defects increases with the square root of the power ($\sqrt{P}$). This last point only holds true if the defect response is situated in the signal linearity zone. As a result, power response curves were carried out to estimate the linearity zone of the control samples and the different defects studied, as well as to analyze the defects of the samples in this power range.

$$I_{norm} = \frac{I.T}{G.\eta.Q.g^2.P^{1/2}H_m.S(S+1)} \quad \textbf{Eq. 1}$$

$$N_{spin} = N_{ref}.\frac{I_{norm}}{I_{norm}^{ref}} \quad \textbf{Eq. 2}$$

$$C_{spin} = \frac{N_{spin}}{m_{sample}} \quad \textbf{Eq. 3}$$

where: *I* is the double integral of the signal associated with a defect; *T* the temperature (K); *G* the gain of the spectrometer; η: the filling factor; *Q* the quality factor; *g*: the Landé factor of the defect; *P*: the power; H_m the modulation amplitude; *S* the spin of the paramagnetic defect; and m_{sample} the mass of the sample.

In practice, η and Q are considered equal in all the samples. Taking the Landé factor g into consideration is open to debate. Although this parameter is constant for the isotropic defects, it is tensorial in nature for the non-isotropic defects. Accordingly, most defects are characterized by three main components g_x, g_y and g_z. However, it is difficult to implement corrections for the non-isotropic defects. The three main components of the defects during the study were quantified with values between 2.15 and 1.99. Given the small variation range of these values, it was decided to consider the parameter g as being identical for all the defects.

Two control samples were used in this study. The first was a sample of alanine irradiated at 6.7 kGy via gamma radiation. This dose value was selected because the production of paramagnetic defects in alanine varies linearly up to a dose of 10 kGy.[20–22] A number of authors have suggested radiolytic yields associated with this production of defects. For example, Nakagawa *et al.*[23] indicated a yield of 0.42 μmol.J^{-1} at 2.7 kGy and 0.52 μmol.J^{-1} at 11 kGy; Gottschall *et al.*[24] a production yield of 0.34 μmol.J^{-1} ; and Van Laere *et al.* a value of 0.43 μmol.J^{-1}.[21] A value of 0.40 μmol.J^{-1} matching the average of the data available in the literature was chosen for this study.

The second control sample consisted of L.P. portlandite powder, which contains manganese Mn^{2+} highly visible in EPR. An assay by ICP-MS was used to estimate the manganese content at 15 ppm in this powder (Table 1). Based on the assumption that all the manganese was in the form of Mn^{2+} ions replacing Ca^{2+} ions in the crystal structure, it was possible to use a non-irradiated sample of $Ca(OH)_2$ L.P. as the control.

The calculation of the normalized double integral I_{norm} (**Eq. 1**) was performed on the two control samples in order to validate this approach. The spectra used as the basis for the I_{norm} calculations were recorded under similar conditions, and a difference of only 7% was observed in each case. The two methods, therefore, produce consistent results.

Data processing. The analysis and processing of the EPR measurement data were carried out using EasySpin software (Toolbox Matlab).[25,26] This tool includes functions for simulating EPR spectra. The software also uses least-squares minimization to optimize a theoretical spectrum in relation to a given experimental spectrum. The value of the Landé factors, the relative intensity of the different signals, the presence of hyperfine coupling, etc. are all parameters that can be varied. When a spectrum consists of several superimposed signals, the Landé g_i factors of the various defects were established by optimization.

Results

Irradiation in liquid nitrogen. Samples of U.P. portlandite were irradiated in liquid nitrogen for doses of between 5 and 120 kGy with the aim of studying the highly reactive species formed on exposure to irradiation. After irradiation - and without breaking the cold chain - EPR spectra were recorded at a temperature of -150°C. **Fig. 2a** sets out the EPR spectrum of a portlandite sample irradiated at 20 kGy in liquid nitrogen. The spectrum is for the most part dominated by an axially symmetric defect, for which the components $g_{\perp}$ = 2.0756 and $g_{/\!/}$ = 2.0017 were identified. This defect, which is attributed to $CaO^{\bullet}$,[13,27] is due to the presence of a hole on an oxygen atom. In addition, the spectrum had a faint, almost isotropic signal at g = 1.9997. According to Barsova *et al.*,[13] this is almost certainly an electron that is trapped and localized on the surface of the material. Moreover, we observed a large difference between the saturation curve of the trapped electron (saturation observed at a lower power) and those of other radicals, such as $CaO^{\bullet}$ (see **Fig. S3** in the Supporting Information). This, while not definitively proving that the trapped electrons are localized at the surface, does indicate a longer spin-lattice relaxation time, as expected for a defect localized at the surface. The trapped electron $e^{-}_{trapped}$ corresponds to an electron localized in a hydroxide vacancy on the surface of the material. The missing hydroxide group $OH^{-}$is then replaced by an unpaired electron. Similar defects with a comparable signature have been identified and studied in MgO.[28,29] The existence of a hydroxide vacancy may be due to irregularities on the surface areas of the material[30,31] or to a slight dehydroxylation during the thermal treatment used to desorb the water.

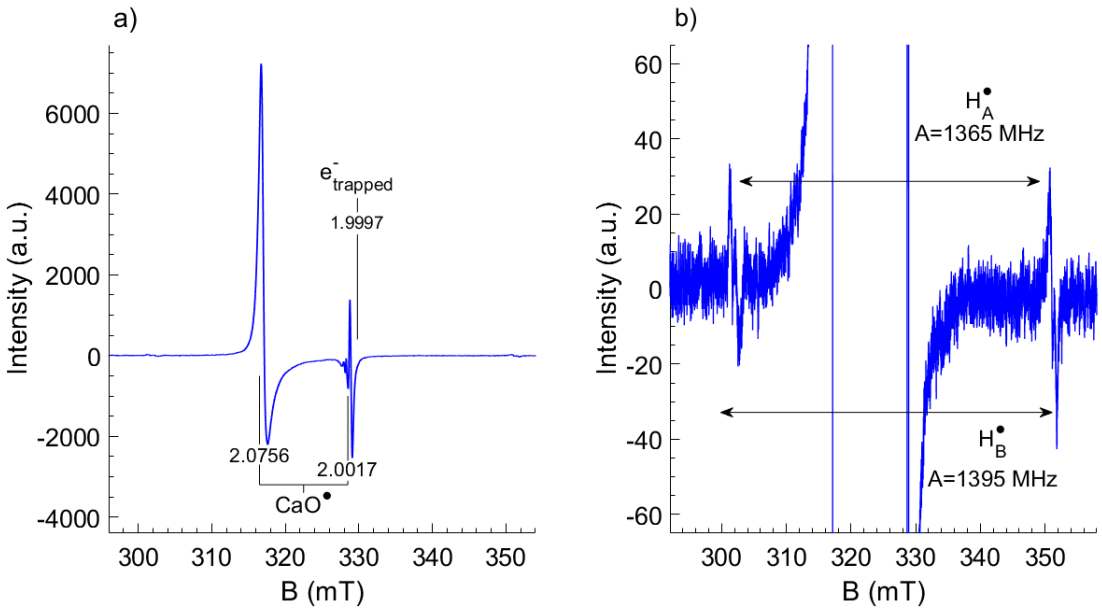

***Fig. 2**. EPR spectrum of a U.P. portlandite sample irradiated at 20 kGy in liquid nitrogen. a) Total spectrum: the Landé factors corresponding to the axial signal from the $\boldsymbol{CaO^{\bullet}}$ radicals and the quasi-isotropic signal $\boldsymbol{e^{-}_{trapped}}$ are shown. b) Magnification and illustration of two signals belonging to the $\boldsymbol{H^{\bullet}}$ radicals. The spectrum was recorded at a temperature of -150°C and a power of 0.01 mW.*

A magnification on the y-axis (**Fig. 2b**) reveals a low signal intensity with a hyperfine interaction with an atom of nuclear spin *I = 1/2*. This characteristic signal is due to the presence of $H^{\bullet}$ radicals. Although the signal associated with $H^{\bullet}$ radicals was faint, it was possible to analyze and model it using the EasySpin software.[25] The best simulation obtained of this signal suggests that it is actually made up of two signals with different hyperfine coupling constant values. The existence of two types of $H^{\bullet}$ radicals in irradiated portlandite has already been reported by Barsova.[15] The coupling constants calculated here were 1365 MHz and 1395 MHz (**Fig. 2b**), values that are consistent with those of 1366 MHz and 1412 MHz reported by Barsova *et al.*[15] The presence of two signals suggests that the $H^{\bullet}$ radicals coexist in distinct chemical environments. The low intensity of the signals, however, prevents a more detailed analysis from being carried out. The abundant quantities of $H^{\bullet}$detected by Barsova *et al.* stem from the fact that the authors were able to record the EPR spectra at -196°C,[15] while the apparatus used here means it was not possible to reach temperatures below -150°C. The main defects detected after irradiation in liquid nitrogen and EPR detection at -150°C are detailed in **Table 2**. Note that, in the case of the trapped electron, the observed behavior of the g-values (which are not isotropic) could be due to the local structure of the trapping site, or to a small structural relaxation taking place after the electron trapping process, apart from reflecting specific properties of the electrons trapped on the surface.

Table 2. *EPR defects identified after $Ca(OH)_2$ irradiation in liquid nitrogen and EPR analysis at -150°C. The values given are those used to simulate the total signal. They are consistent with those given in the references cited.*

Defects	g_x	g_y	g_z	A (MHz)	Reference
$CaO^{\bullet}$	2.0756		2.0017	*Ø	[13,27]
e^-_{trapped}	2.0003		1.9997	*Ø	[13]
$H_A^{\bullet}$	2.0029			1365	[15]
$H_B^{\bullet}$	2.0027			1395	[15]

**No hyperfine coupling*

The irradiation of samples of U.P.-L.S. portlandite (**Fig. S4 in Supporting Information**), with a similar composition but lower specific surface area than U.P. portlandite, demonstrated the existence of $CaO^{\bullet}$ radicals but only minor amounts of trapped electrons. The existence of $CaO^{\bullet}$ radicals, and in similar proportions for U.P. and U.P.-L.S. portlandite, suggests a localization of these species in the volume of the material. On the other hand, the low presence of radicals e^-_{trapped} in the U.P.-L.S. portlandite is compatible with the surface localization put forward by Barsova.[13]

The evolution of the concentration of the $CaO^{\bullet}$ radicals and e^-_{trapped} with the dose delivered to the samples is set out in **Fig. 3.** The evolution of the concentration of the $CaO^{\bullet}$ radicals is linear between 0 and 120 kGy. The concentration in e^-_{trapped} shows a maximum at 20 kGy before decreasing with the dose delivered. Although the position of the maximum differs, the overall shape of the concentration curve in e^-_{trapped} as a function of the dose is similar to that determined by Barsova.[13] The radiolytic yield of the production of the $CaO^{\bullet}$ radicals was estimated by measuring the slope of the line. For $e^-_{trapped}$, the radiolytic yield $G(e^-_{trapped})$ was estimated using the slope of the curve calculated between 0 and 20 kGy (**Fig. 3)**. For the $CaO^{\bullet}$ radicals, their localization in the volume means it is easier to compare the different studies with one another. Accordingly, a value of $G(CaO^{\bullet}) = 4.3 \times 10^{-8}$mol.J^{-1} was found. This value is approximately half that found by Barsova *et al.*[13] We should note, however, that the irradiations by Barsova *et al.* were performed with gamma radiation, while the samples here were irradiated with accelerated electrons, i.e. radiation with entirely different dose rates, which might explain the factor of 2 between the values obtained. The comparison of $G(e^-_{trapped})$ is harder since this species is localized on the surface of the material, which implies that there is a correlation with

the specific surface area of the samples. A yield $G(e^-_{trapped}) = 7\times10^{-9}\ mol.J^{-1}$ was calculated. This value represents a third of that measured by Barsova.[13] It should be noted that the study by Barsova *et al.* [13] mentions samples with a specific surface area of 30-40 $m^2.g^{-1}$ compared to approximately 15 $m^2.g^{-1}$ here. This difference may in part explain the difference in yield between the two studies.

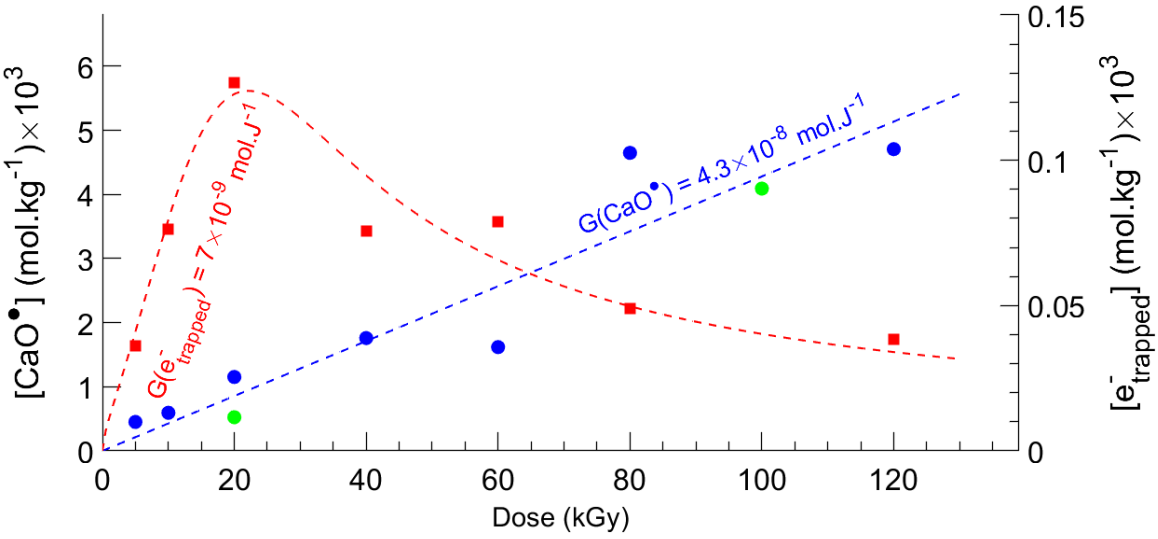

Fig. 3*. Evolution of the concentration of* $\boldsymbol{CaO^{\bullet}}$ *radicals (blue and green circles for U.P. and U.P.-L.S. samples, respectively) and* $\boldsymbol{e^-_{trapped}}$ *(red squares) after irradiation by accelerated electrons in liquid nitrogen of the U.P. and U.P.-L.S. portlandite samples. The alanine irradiated at 6.7 kGy was used to calculate the number of spins. Each point was derived from an independent sample. The EPR spectra were recorded at a temperature of -150°C and a power of 0.01 mW.*

The $CaO^{\bullet}$ radicals and $e^-_{trapped}$ are only stable at low temperatures. Observing them required irradiation in liquid nitrogen followed by analysis at low temperature. Using the EPR thermal regulation device, the kinetics of disappearance of these two radicals was measured for temperatures between -80°C and 0°C. **Fig. 4** sets out the evolution of the normalized intensity of these two defects over time. The disappearance of the $CaO^{\bullet}$ radicals (**Fig. 4a**) can be modeled by kinetics of order 2, which results in the following evolution of their concentration as a function of time (**Eq. 4**):

$$\frac{[CaO^{\bullet}]_t}{[CaO^{\bullet}]_0} = \frac{1}{1 + k.[CaO^{\bullet}]_0.t} \qquad \textbf{Eq. 4}$$

where *t* is time (in minutes) and *k* the rate constant associated with the reaction. Note that the annealing data are well fitted by the homogeneous kinetics equations.

The plot of *ln(k)* as a function of the temperature shows that *k* follows an Arrhenius law $k = k_0.exp(-E_a/RT)$ with activation energy E_a = 30.5 kJ.mol^{-1} (**Fig. S5 in Supporting Information**).

On the other hand, studying the kinetics of $e^-_{trapped}$ did not make it possible to demonstate a specific order of the reaction. In particular, the annealing temperatures of 0°C and -20°C resulted in disappearances of $e^-_{trapped}$ that were too fast to be measured.

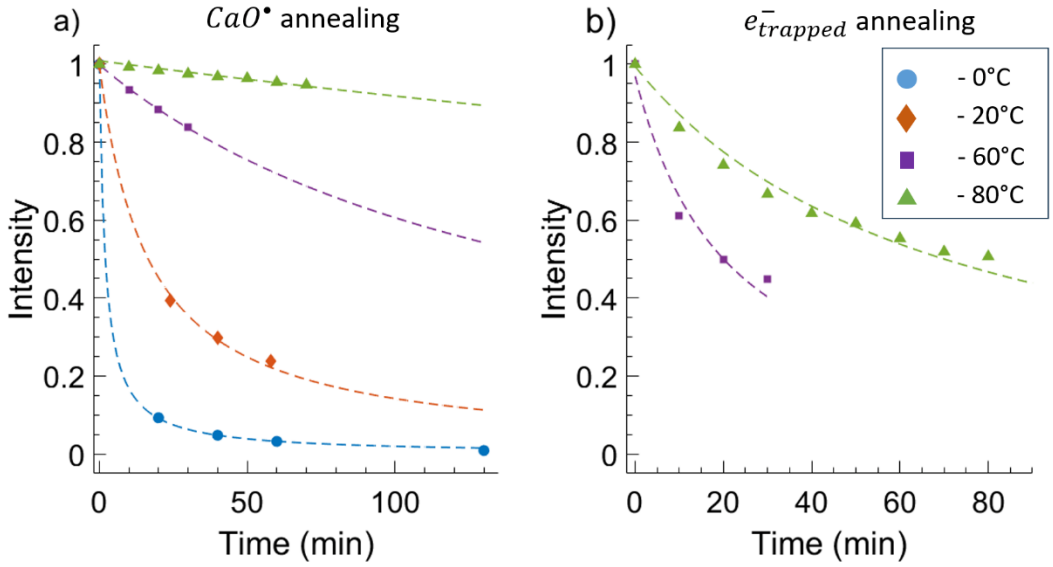

Fig. 4. *Kinetics of disappearance of* $\boldsymbol{CaO^{\bullet}}$ *radicals and* $\boldsymbol{e^-_{trapped}}$ *in the U.P. portlandite. a) Evolution of the normalized intensity of the EPR signal associated with the* $\boldsymbol{CaO^{\bullet}}$ *radicals in the portlandite annealed at various temperatures. The dotted curves represent kinetic modeling of order 2. b) Evolution of the normalized intensity of the EPR signal associated with* $\boldsymbol{e^-_{trapped}}$ *in the portlandite annealed at various temperatures. The experimental spectra were recorded at a power of 1 mW.*

The disappearance of radical signals $CaO^{\bullet}$ is followed shortly afterwards by the appearance of a new EPR signal. This quasi-axial signal has a component g_x = 2.1476, which is also observed if the samples are irradiated at room temperature (**Fig. 5**). Even if the defect responsible for the new signal is resistant to ambient temperature, it is only visible if the EPR analysis is carried out at a temperature below -100°C (**Fig. 5**). It should be noted that signals of similar shape were observed in the irradiated oxides CaO and MgO and were associated respectively with the

superoxide radical $CaO_2^{\bullet}$ and $MgO_2^{\bullet}$.[32–34] It seems reasonable, therefore, to tentatively attribute this new signal to the formation of $CaO_2^{\bullet}$ although the value of g_x reported in ref 35 is different.

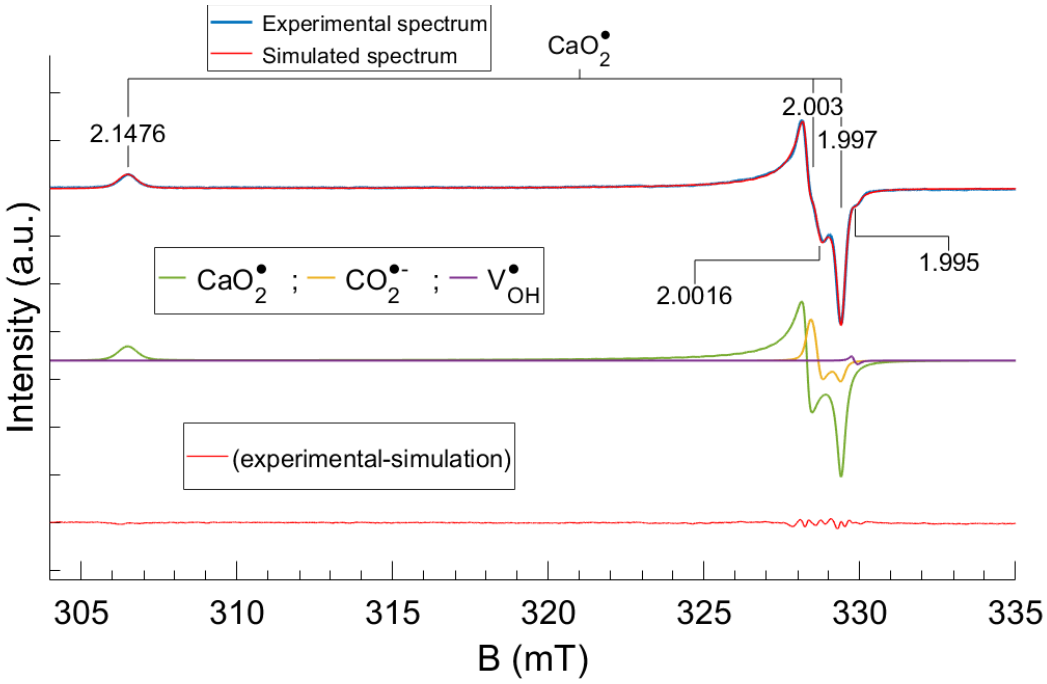

Fig. 5. *Decomposition of the spectrum of a U.P. portlandite sample irradiated in liquid nitrogen at 40 kGy, annealed at room temperature and analyzed by EPR at -150°C. Uppermost line: experimental spectrum (solid blue line) and overall modeling (dotted red line); middle lines: decomposition of the contributions of the different defects present in the overall spectrum; bottom line: residual (difference between the experimental spectrum and the modeling). The experimental spectrum was recorded at a power of 1 mW.*

The decomposition of the spectrum and its optimization demonstrated the presence of three defects (**Fig. 5**). Although most of the spectrum is dominated by the signal belonging to $CaO_2^{\bullet}$, another signal almost certainly belonging to the radical $CO_2^{\bullet-}$ is also present.[36,37] That this radical is present is of no surprise since the samples all contain a small quantity of calcite ($CaCO_3$). The third signal is quasi-isotropic and of very low intensity. By analogy with what was observed in ZnO, it is possible that it is a single electron trapped in a vacancy located in the volume of the material.[38–40] This interpretation is compatible with the isotropic nature of the signal and the low value of the related Landé factor (less than 2). Accordingly, and even though no clear identification was possible, it could be an electron trapped in a vacancy $V_{OH}^{\bullet}$ (or electron occupying the place of a hydroxide group) located in the volume of the material. The Landé factors of the three defects identified in **Fig. 5** are given in **Table 3**.

Table 3*. EPR defects identified after portlandite irradiation at 40 kGy in liquid nitrogen, annealed at room temperature, and EPR analyzed at -150°C. The* $\boldsymbol{CO_2^{\bullet-}}$ *radical is shown as* $\boldsymbol{CO_2^{\bullet-}(1)}$ *in the table to differentiate it from another radical of the same type, observed and identified in the text below (see Table 4).*

Defects	g_x	g_y	g_z	Reference
$CaO_2^{\bullet}$	2.1476	2.004	1.9974	[32–34]
$CO_2^{\bullet-}(1)$	2.0032	2.0017	1.9974	[36,37]
$V_{OH}^{\bullet}$	1.995			[38–40]

Irradiation at room temperature. EPR measurements were also performed on portlandite samples irradiated at room temperature. **Fig. 6** (blue curve) shows the EPR spectrum of a portlandite sample irradiated at 120 kGy at room temperature. The spectrum consists of several signals that are hard to identify. A thermal treatment at 50°C was performed (**Fig. 6a**) in order to simplify the spectrum. With this treatment, it is possible to selectively attenuate the signal of some defects. **Fig. 6b** shows the spectrum of defects that disappeared during annealing at 50°C. This spectrum is obtained by subtraction of the reference spectrum with the spectrum measured after the sample has remained at 50°C for 4 hours. It is then possible to identify the defects that make up this spectrum. Evidently, a substantial portion comes from the calcite present in the material in small quantities (**Table 4**).

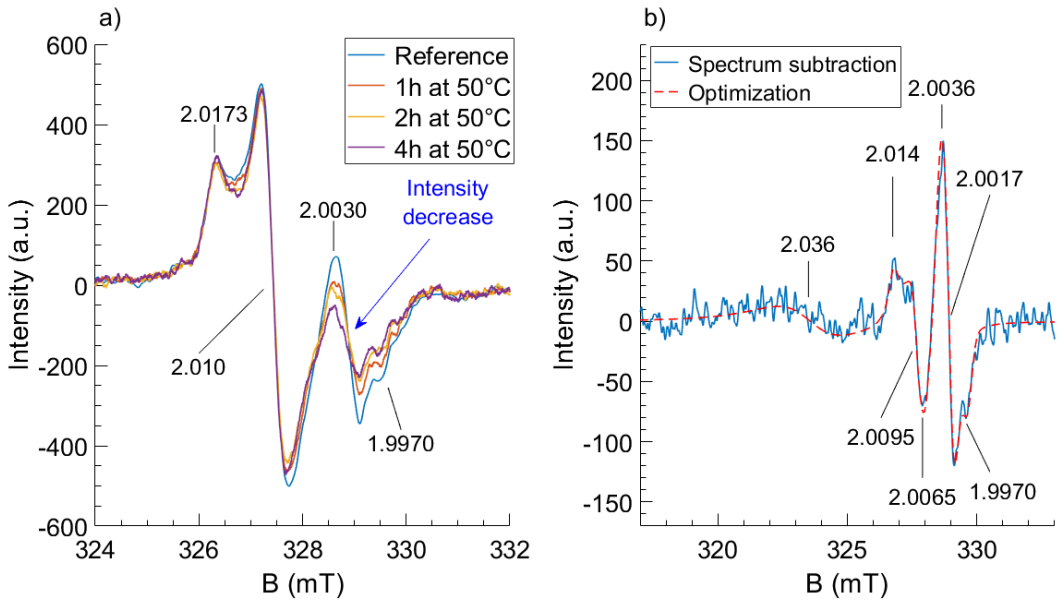

Fig. 6. *Illustration of the paramagnetic defects by annealing at 50°C of a sample of U.P. portlandite irradiated at 120 kGy. a) Evolution of the spectrum with the duration of annealing at 50°C. The spectra were recorded at a power of 4 mW and at room temperature. b) (Blue line): subtraction of the reference spectrum and the spectrum obtained after the sample remained for 4 hours at 50°C. (Red dotted line): spectrum optimized with EasySpin software.*

Furthermore, the use of a thermal treatment at 180°C for 10 minutes further simplified the EPR spectrum and eliminated the defects linked to the presence of calcite in their entirety (**Fig. 7a**). The spectra of **Fig. 7a** are then for the most part made up of two signals, including one that is quasi-isotropic at $g \approx 2.010$. When the thermal treatment is performed at 180°C for several hours (**Fig. 7**), an increase in the intensity of this signal is observed. On the other hand, the shoulders at $g = 2.0173$ and $g = 2.003$ decrease. It is possible to isolate the quasi-isotropic signal (**Fig. 7b**) by subtracting the different spectra.

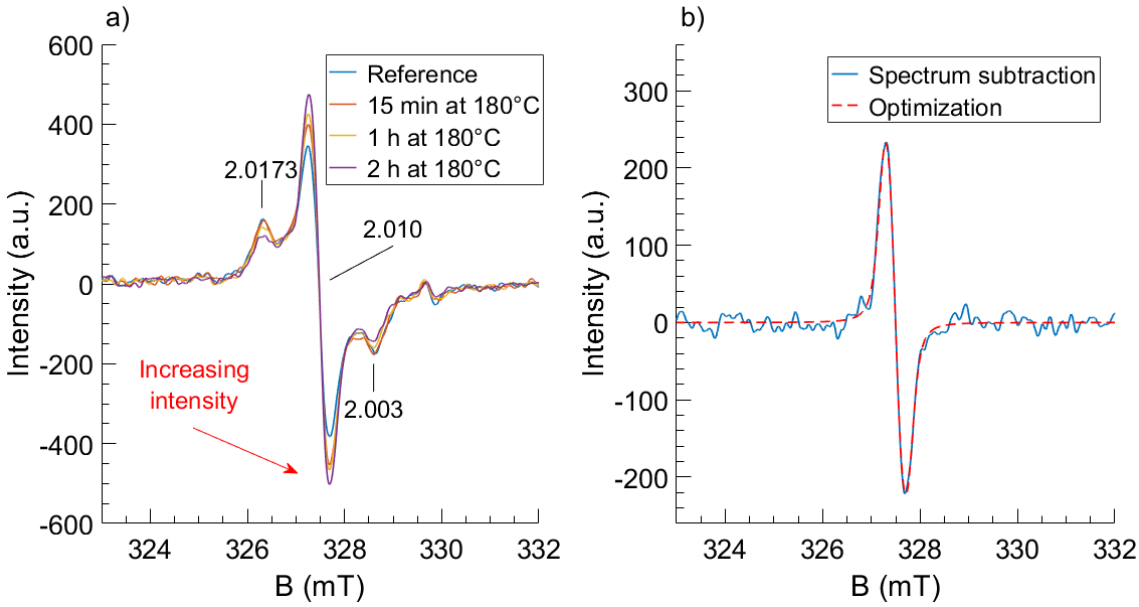

Fig. 7. *Illustration of the paramagnetic defects present in the spectrum via annealing experiments at 180°C of a sample of U.P. portlandite irradiated at 120 kGy at room temperature. a) Evolution of the spectra with the duration of annealing at 180°C. Spectra recorded at room temperature and a power of 4 mW. b) (Blue line): subtraction of the control spectrum and the spectrum obtained after heating for 2 hours at 180°C. The two spectra were normalized in intensity on the component at g = 2.0173 in order to eliminate the shoulders at 2.0173 and 2.003. (Red dotted line): Spectrum optimization using EasySpin software.*

The simulation of the spectrum determined the Landé factors of the isolated signal (**Fig. 7b**): $g_x = 2.0114$; $g_y = 2.0104$; $g_z = 2.0085$. It was then possible to identify the other defect present in the spectrum, and whose Landé factors were as follows: $g_x = 2.0173$; $g_y = 2.010$; $g_z = 2.003$ (**Fig. 7a**). **Table 4** gives an overview of all the defects detected at room temperature together with their probable attribution.

Table 4. *Paramagnetic defects identified in the portlandite irradiated at room temperature.*

Defects	**g_x**	**g_y**	**g_z**	**Specificities**	**References**
$CO_2^{\bullet -}(1)$	2.0008				[36,37]
$CO_2^{\bullet -}(2)$	2.0036	2.0017	1.9970		[36,37]
$CaO_3^{\bullet}(1)$	2.014	2.009	2.007		[41]
$CaO_3^{\bullet}(2)$	2.0173	2.010	2.003		[33]
*RD_1	2.0114	2.0104	2.0085	Not localized on an oxygen atom	

$CaO_2^{\bullet}$	2.01476	2.004	1.9974	Visible if T< -100°C	[32–34]
$V_{OH}^{\bullet}$	1.995-1.996				[38,39]
*RD_2	2.036		2.002	Linked to the presence of carbonate	

**Where it was not possible to make a precise attribution, the name RD_i (for radiation-induced defect n°i) has been used.*

An analysis of the literature failed to attribute the signal corresponding to the quasi-isotropic defect RD_1 (with RD signifying "radiation-induced defect"; see **Table 4**). One should note, however, that a relatively similar defect with a Landé factor g_{iso} = 2.012 was observed in the case of aluminum hydroxides.[42] Although no clear attribution was given, membership to a type of ozonide radical is suggested by Kaddissy *et al.*[42] A portlandite specially enriched in ^{17}O was made in order to test this hypothesis. No hyperfine coupling was observed on the isotropic signal (**Fig. S6 in Supporting Information**). This suggests that the defect is not localized on an oxygen atom; it excludes the fact, therefore, that it is a $CaO_3^{\bullet}$ radical. It follows that the localization of the quasi-isotropic defect on a metallic impurity is the most likely explanation. In fact, some metallic impurities such as Pb^{3+} are known to give an isotropic signal with a similar Landé factor.[43] In addition, we should note that the $CO_2^{\bullet -}(1)$ radical (**Table 4**) is the same as the one detected at -150°C (**Table 3**). In addition, when the measurement is performed at room temperature, the components of the Landé factor are averaged and the defect becomes quasi isotropic with a Landé factor g_{iso} = 2.0008.

Metallic impurities. The results above apply to the U.P. portlandite powder with a low metal impurity content. Room-temperature irradiations were also performed on L.P. portlandite samples containing more elements present in low quantities. As a result, the EPR analysis of a non-irradiated sample made it possible to demonstrate the existence of metallic impurities. **Fig. 8** shows the evolution of the EPR signal of the metal impurities identified prior to and following irradiation at 20 kGy. The signal at $g = 4.25$ is a well-known signal belonging to Fe^{3+},[44,45] and the one at g = 5.1 belongs to Cr^{3+}.[46,47]

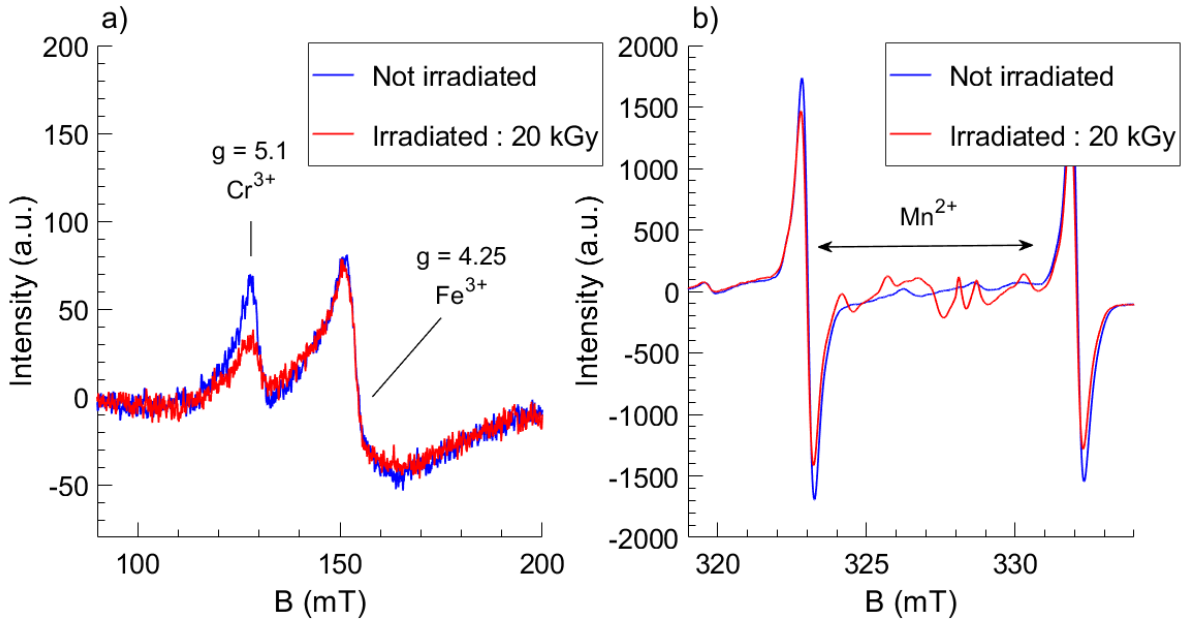

Fig. 8. *Influence of irradiation at 20 kGy at room temperature on the quantities of* $\boldsymbol{Cr^{3+}}$, $\boldsymbol{Fe^{3+}}$ *and* $\boldsymbol{Mn^{2+}}$ *contained in L.P. portlandite. (Blue line): non-irradiated L.P. portlandite; (red line): sample irradiated at 20 kGy. a) Low-field magnification on the signal of* $\boldsymbol{Cr^{3+}}$ *and* $\boldsymbol{Fe^{3+}}$*; b) high-field magnification on two peaks belonging to* $\boldsymbol{Mn^{2+}}$*. The spectra were recorded at a power of 1 mW.*

A reduction in the content of Cr^{3+} by 60% (**Fig. 8a**) and Mn^{2+} by 20% (**Fig. 8b**) was observed after irradiation at 20 kGy. This shows that irradiation alters the degree of oxidation of the different impurities present in the portlandite. The Fe^{3+} content did not change. We should note, however, that the presence of Fe^{3+} is due at least in part to the tubes used, which contain up to 1200 ppm of Fe_2O_3 (manufacturer's data).

The experimental data in its entirety can be used to propose different reactions occurring in irradiated portlandite and to create a reaction diagram so we can understand the origin of the immediate and delayed production of molecular hydrogen in this type of compound. Several types of carbonate radicals were illustrated among the recorded species. As these species do not seem to be involved in producing molecular hydrogen under irradiation, they will not be discussed subsequently.

Discussion

Although there are a number of studies on the EPR analysis of metal oxides,[9–12] there are comparatively few on the defects present in hydroxides. The chemical proximity of hydroxides and oxides will mean, however, that we adopt the same notation. For reasons of simplicity and

representation, it is practical to regard calcium hydroxide as a mono-charged calcium ion linked to an anionic oxygen, which is itself linked to a proton: $Ca^{+} - O^{2-} - H^{+}$. In this convention, the association of Ca^{+} with the radical $O^{\bullet -}$ will be noted $CaO^{\bullet}$, an electrically neutral and paramagnetic entity.

Surface reactions

We will focus here especially on very reactive species such as $CaO^{\bullet}$, $e^{-}_{trapped}$ and $H^{\bullet}$ that are involved in the production/destruction phenomena of radiolytic H_2. We should remember that, experimentally, irradiated portlandite results in the immediate production of molecular hydrogen, and that a portion of the created molecular hydrogen remains trapped within the material, leading to delayed production.[8] As the immediate production increases with the material's specific surface area, it may be imputed to reactions occurring on the surface, in contrast to trapped molecular hydrogen, which is formed via reactions taking place within the volume of the material.[8]

At the beginning of the radiation/matter interaction, electron/hole pairs are created in the material (**R. 1**). We can then explain the creation of $CaO^{\bullet}$ by the capture, by an oxygen atom, of a hole h^{+}(**R. 2**), while the trapped electrons can result from the capture of an electron on a surface site of the portlandite (**R. 3**).

$$Irradiation \rightsquigarrow e^{-} + h^{+} \qquad \textbf{R. 1}$$

$$CaOH + h^{+} \rightarrow CaO^{\bullet} + H^{+} \qquad \textbf{R. 2}$$

$$e^{-} + surface \rightarrow e^{-}_{trapped} \qquad \textbf{R. 3}$$

The H^{+} proton produced by the reaction **R. 2** is not paramagnetic; as a result, it is not detectable by EPR. The combination of reactions **R. 1 - R. 3** must in theory produce an equivalent quantity of electrons $e^{-}_{trapped}$ and $CaO^{\bullet}$ radicals. As can be seen in **Fig. 3**, the quantity of electrons detected is much lower than the quantity of $CaO^{\bullet}$ radicals. We may assume, therefore, that there is a rapid recombination reaction of a portion of the protons and electrons to form the radical $H^{\bullet}$:

$$H^{+} + e^{-} \rightarrow H^{\bullet} \qquad \textbf{R. 4}$$

It should be noted that the recombination of a hole and an electron formed by the reaction **R. 1** may also create an excitonic mechanism (**R. 5** & **R. 6**). DFT calculations have recently shown

that it was possible for an exciton to be created in minerals such as $Ca(OH)_2$ and $Mg(OH)_2$.[48] This means of energy transfer is well known in silica, where it may result in the creation of $H^\bullet$ radicals.[49]

$$e^- + h^+ \rightarrow exciton \qquad \textbf{R. 5}$$

$$CaOH + exciton \rightarrow CaO^\bullet + H^\bullet \qquad \textbf{R. 6}$$

Although the ionic mechanism may be positively identified thanks to the observation of $e^-_{trapped}$, the excitonic mechanism is more uncertain. In all cases, without taking into account reactions additional to **R. 1 - R. 6**, the following equality is expected to be observed:

$$n(CaO^\bullet) = n(H^\bullet) + n(e^-) \qquad \textbf{Eq. 5}$$

In practice, **Eq. 5** is never respected. In fact, the quantity of $e^-_{trapped}$ and $H^\bullet$ is much lower than that of the $CaO^\bullet$ radicals. This deficit could be explained by the highly reactive species quickly resulting in the formation of molecular H_2 that cannot be detected by EPR.

Several reaction mechanisms have been conceived of to explain the formation of molecular H_2. Immediate H_2, which is released very quickly during irradiation, is the outcome of mechanisms that take place on the surface of the material. The existence of surface mechanisms stems from the fact that the proton H^+ and electron e^- are highly mobile in the solid, regardless of the fact that the surface area is a topologically specific location. We should remember that EPR-detected $e^-_{trapped}$ is consistent with electrons trapped on the surface of the material (**Fig. 2**). A calculation, described in the Supporting Information (see **Calculating the number of surface sites in Supporting Information**), was used to estimate the number of O-H bonds on the surface of the U.P. portlandite at 1.1×10^{-1} mol.kg^{-1}. If we factor in a maximum $e^-_{trapped}$ concentration of $1{,}3 \times 10^{-4}$ mol.kg^{-1} (**Fig. 3**), this suggests that approximately 1/1000 of the surface bonds corresponding to a surface site stabilize an electron. The surface's ability to stabilize electrons means it is potentially a special reaction site via the following reactions:

$$H^+ + e^-_{trapped} \rightarrow H^\bullet_{surface} \qquad \textbf{R. 7}$$

$$H^\bullet_{surface} + H^\bullet_{surface} \rightarrow H_{2(g)} \qquad \textbf{R. 8}$$

$$H^\bullet_{surface} + CaOH_{surface} \rightarrow H_{2(g)} + CaO^\bullet_{surface} \qquad \textbf{R. 9}$$

It is thus possible to conceive of a mechanism for producing H_2 via the dimerization of $H^\bullet_{surface}$ radicals (**R. 8**). It should be noted that a formation reaction by abstraction, involving a single

radical $H^{\bullet}$(**R. 9**), is also possible, and has been suggested in the case of aluminum hydroxides.[50] The surface formation of $H_{2(g)}$ by the reactions **R. 8** and **R. 9** account for this immediate production of H_2, which is even higher since the samples have a substantial specific surface area.[8]

As can be seen in **Fig. 3**, the concentration of $e^-_{trapped}$ decreases with the absorbed dose above 20 kGy. This saturation phenomenon is consistent with an immediate surface production that is initially stimulated but that diminishes as and when the sites enabling surface stabilization run out. This phenomenon explains the gradual decrease in the immediate production of H_2 as observed in the study by Herin *et al.*[8]

One possible pathway of disappearance of surface vacancies is a reaction with a $CaO^{\bullet}$ radical near the surface.

$$CaO^{\bullet} + e^-_{trapped} \rightarrow Ca - O^- \qquad \textbf{R. 10}$$

$$Ca - O^- + H^+ \rightarrow CaOH \qquad \textbf{R. 11}$$

Accordingly, the disappearance of the surface hydroxide vacancies that enable electron stabilization could be the outcome of the reformation of CaOH bonds.

Herin *et al.*[8] have stated that L.P. portlandite did not produce immediate H_2 for doses between 0 and 30 kGy. This non-production was not observed in the U.P. portlandite. It is reasonable, therefore, to attribute this difference in behavior to the presence of impurities in the L.P. portlandite. The reduction in the content of $Cr^{3+}$of 60% after 20 kGy seems consistent with an H_2 production that becomes measurable from 30 kGy in the L.P. portlandite (**Fig. 8).** Although it was not possible to demonstrate the presence of Cr^{2+}, Cr^{3+} without a doubt traps the electrons (**R.** *12*), which inhibits the surface production mechanism of H_2 (**R. 8** and **R. 9**).

$$Cr^{3+} + e^- \rightarrow Cr^{2+} \qquad \textbf{R. 12}$$

The reduction in the content of $Mn^{2+}$of approximately 20%, which was also observed, would seem to be too low to explain the absence of H_2 production between 0 and 30 kGy. Nonetheless, these observations show that manganese changes its level of oxidation during irradiation and, therefore, is instrumental in capturing the reactive species created during irradiation (**Fig. 8**). It should be noted that a real material would contain impurities in much higher proportions than in the materials studied in this work.

Reactions in the volume

The immediate H_2 derived from surface reactions is not the only type of H_2 produced during irradiation. In fact, reference [8] showed that a portion of the H_2 produced during irradiation remains trapped in the material. This $H_{2(trapped)}$ is almost certainly due to the reaction mechanisms occurring in the volume of the material. As for immediate H_2, $H_{2(trapped)}$ stems from the dimerization (**R. 13**) or abstraction reaction of the (**R. 14**) $H^{\bullet}$ radicals that occur in the volume of the material.

$$H^{\bullet} + H^{\bullet} \rightarrow H_{2\,(trapped)} \qquad \textbf{R. 13}$$

$$H^{\bullet} + \ CaOH \rightarrow CaO^{\bullet} + H_{2\,(trapped)} \qquad \textbf{R. 14}$$

It should be noted that even if the rate constant of **R. 13** is far lower than for **R. 14**, the second reaction (**R. 13**) may nonetheless be the reaction that for the most part results in the formation of H_2 due to the concentration of CaOH species in the crystal lattice, which is very much greater than for the $H^{\bullet}$ radicals. Accordingly, the reactions **R. 13** and **R. 14** give rise to the production of $H_{2(trapped)}$ with very little mobility, which stays trapped for the most part in the material.

This accumulation of $H_{2(trapped)}$ cannot carry on indefinitely, however, since the oxidizing species produced by the irradiation gradually reduce the production of H_2.

While it is obvious that the recombination reaction **R.** *15* plays a role in reducing the H_2 production, this reaction cannot be entirely responsible on its own.

$$H^{\bullet} + \ CaO^{\bullet} \rightarrow CaOH \qquad \textbf{R. 15}$$

In particular, the disappearance of $CaO^{\bullet}$ radicals based on second-order kinetics (**Fig. 4**) occurs without further modification of the EPR spectrum, suggesting the formation of a diamagnetic species (**R. 13**) - namely, peroxide $CaO - OCa$:

$$CaO^{\bullet} + \ CaO^{\bullet} \rightarrow \ CaO - OCa \qquad \textbf{R. 16}$$

The capacity of $CaO^{\bullet}$ radicals to react with one another via **R.** *16* assumes a degree of mobility on their part in the crystal structure. This mobility may be explained by the fact that in reality it is the hydrogen atoms that move by jumping on the Wyckoff sites:[51,52]

$$CaO^{\bullet} + H - OCa \ \rightarrow \ CaO - H + \ O^{\bullet}Ca \qquad \textbf{R. 17}$$

It should be noted that a disappearance of $CaO^{\bullet}$ radicals by reaction with a molecule of $H_{2(trapped)}$ in the material is equally possible (**R.** *18*). In fact, the radicals can only react with a trapped molecular hydrogen molecule since the molecular hydrogen molecules formed on the material's surface are released immediately into the gaseous atmosphere.

$$H_{2(trapped)} + CaO^{\bullet} \rightleftarrows CaOH + H^{\bullet} \qquad \textbf{R. 18}$$

The reaction **R.** *18* is then rounded off by the reaction **R.** *15* enabling the $H^{\bullet}$ radicals formed to be consumed quickly.

It is highly likely that the $CaO^{\bullet}$ radicals are more mobile than the molecules of $H_{2(trapped)}$. The high degree of mobility of the $CaO^{\bullet}$ implies that the reaction **R.** *16* is almost certainly the majority pathway of disappearance of the radical $CaO^{\bullet}$ at low doses. In fact, low-dose irradiation implies that a small quantity of $H_{2(trapped)}$ is present within the material. The probability of the reaction between two radicals $CaO^{\bullet}$ (reaction **R.** *16*) is, therefore, the most likely outcome at the outset of the irradiation. However, as the quantity of $H_{2(trapped)}$ increases in the material, the probability of a $CaO^{\bullet}$ center reacting with an H_2 molecule via **R.** *18* grows. The existence of the reaction **R.** *18*, which is predominant at high doses, most likely explains why the quantity of $H_{2(trapped)}$ in the study by Herin *et al.* tends towards a maximum.[8]

Several arguments may be advanced to provide evidence that the reaction **R.** *16* is initially privileged compared to the reaction **R.** *18*. Firstly, the value of the total radiolytic yield of H_2 production,[8] is approximately $G\left(H_2^{total}\right) = 2.2 \times 10^{-8}\, mol.J^{-1}$. Based on **Fig. 3**, the production yield $G(CaO^{\bullet}) = 4.3 \times 10^{-8} mol.J^{-1}$. Assuming that the production of one molecule of H_2 involves the production of two $CaO^{\bullet}$ radicals, the relationship $G(H_2^{total}) \approx$ ½ $G(CaO^{\bullet})$ is verified properly at the outset of the irradiation (**Fig. 3**). Since H_2^{total} is measured following irradiation at room temperature, a temperature where the $CaO^{\bullet}$ radicals only survive for a few minutes, the previous equality indicates that the $CaO^{\bullet}$ radicals initially disappear without consuming the molecules of the trapped molecular hydrogen.

Furthermore, the presence of superoxide radicals $CaO_2^{\bullet}$, formed after the disappearance of the $CaO^{\bullet}$ radicals, is easier to explain based on a peroxide $CaO - OCa$. Accordingly, the radical $CaO_2^{\bullet}$ could be due to the reaction **R.** *19*:

$$CaO - OCa \rightleftarrows CaO_2^{\bullet} + V_{OH}^{\bullet}Ca \qquad \textbf{R. 19}$$

It should be noted that **R.** *19* assumes the creation of an equivalent quantity of $CaO_2^{\bullet}$ and $V_{OH}^{\bullet}$, which has never been observed. In fact, if the vacancies $V_{OH}^{\bullet}$ were assumed (**Fig. 5**), the latter exist in much lower quantities than for the $CaO_2^{\bullet}$ radicals. This point can be resolved by taking into consideration the reaction between the electron occupying the vacancy with a radical $CaO^{\bullet}$ (**R.** *20***)**.

$$CaO^{\bullet} + V_{OH}^{\bullet}Ca \rightarrow Ca - O - Ca \qquad \textbf{R. 20}$$

It should be noted that the $CaO_2^{\bullet}$ radical could also be produced by reaction between a metallic impurity M contained in the portlandite and peroxide $CaO - OCa$:

$$CaO - OCa + M \rightleftarrows CaO_2^{\bullet} + Ca^{+} + M^{-} \qquad \textbf{R. 21}$$

The formation of the ozonide $CaO_3^{\bullet}$ radical is harder to describe. This radical is well known in oxides and is almost always the result of a surface reaction between residual dioxygen $O_{2(g)}$ and the $MO^{\bullet}$ radicals.[32,33,41] By analogy, it is possible to suggest a similar origin to this radical in the portlandite.

$$O_{2(g)} + CaO^{\bullet} \rightarrow CaO_{3(surface)}^{\bullet} \qquad \textbf{R. 22}$$

Recycling mechanisms

It follows that production of molecular hydrogen, which saturates at the highest doses,[8] may have several different origins. The first consists of destruction reactions of the molecular hydrogen molecule (**R. 18**). The second is due to the consumption of the precursors that generate the molecule, such as the hydrogen atom (as **R. 15**). Thus, the reaction **R.** *18* results in internal recycling, which prevents the $H_{2(trapped)}$ accumulating in the material. As explained above, this reaction becomes even more predominant since the dose delivered is large and the quantity of $H_{2(trapped)}$ increases. This limitation of the quantity of $H_{2(trapped)}$ might also be explained by the inhibition of production by the capture of $H^{\bullet}$ radicals. In this context, the reaction between a peroxide and the radical $H^{\bullet}$ (**R.** *23*) is an important reaction for explaining the inhibition of the production of $H_{2(trapped)}$.

$$CaO - OCa + H^{\bullet} \rightarrow CaO^{\bullet} + CaOH \qquad \textbf{R. 23}$$

The different reactions that contribute to the H_2 production mechanism, together with its high-dose recycling, are shown together in **Table 5** below. The reactions that take place on the

surface or in the volume of the material are separated in order to describe the immediate and delayed production of molecular hydrogen respectively. **Fig. 9** shows a summary diagram of the two pathways resulting in H_2 being released into the air.

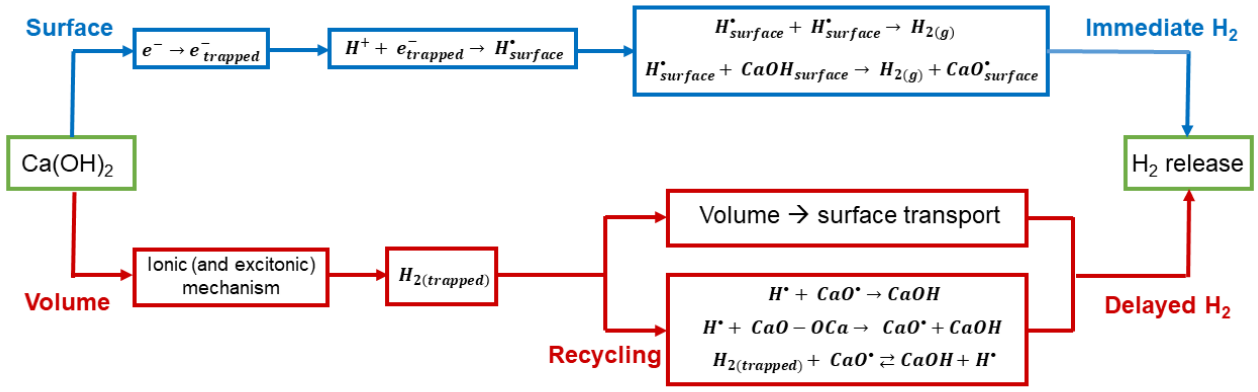

***Fig. 9**. Summary diagram of the volume and surface production mechanisms of the portlandite H_2 exposed to ionizing radiation. The reactions accounting for the saturation of the immediate production of H_2 are not shown in this figure in order to avoid overloading it.*

***Table 5**. (Non-exhaustive) summary of the reaction mechanisms that include H_2 formation and its recycling.*

Localization	No.	Reactions	Type of reactions
COMMON VOLUME AND SURFACE	**R. 2**	$CaOH + h^+ \rightarrow \equiv CaO^\bullet + H^+$	H^+ ion formation
	R. 4	$e^- + H^+ \rightarrow H^\bullet$	radical $H^\bullet$ formation
	R. 13	$H^\bullet + H^\bullet \rightarrow H_2$	H_2 by dimerization
	R. 14	$CaOH + H^\bullet \rightarrow CaO^\bullet + H_2$	H_2 by abstraction
	R. *15*	$CaO^\bullet + H^\bullet \rightarrow CaOH$	recombination 1
	R. *18*	$CaO^\bullet + H_2 \rightarrow CaOH + H^\bullet$	H_2 recycling
	R. *16*	$CaO^\bullet + CaO^\bullet \rightarrow CaO - OCa$	peroxide formation
	R. *23*	$CaO - OCa + H^\bullet \rightarrow CaOH + CaO^\bullet$	peroxide destruction
	R. 10	$CaO^\bullet + e^- \rightarrow CaO^-$	electron capture
	R. 11	$CaO^- + H^+ \rightarrow CaOH$	recombination 2

SURFACE SPECIFIC	**R. 3**	$e^- \rightarrow e^-_{trapped}$	surface trapping
	R. 7	$e^-_{trapped} + H^+_{surface} \rightarrow H^\bullet_{surface}$	counterpart R. 4
	R. 8	$H^\bullet_{surface} + H^\bullet_{surface} \rightarrow H_{2(g)}$	counterpart R. 13
	R. 9	$CaOH_{surface} + H^\bullet_{surface} \rightarrow CaO^\bullet_{surface} + H_{2(g)}$	counterpart R. 14
	R. *23*	$CaO^\bullet_{surface} + O_{2(g)} \rightarrow CaO^\bullet_3$	ozonide formation

Conclusion

Portlandite is a solid that produces H_2 under ionizing radiation. Its behavior is special since, in addition to the immediate production of molecular hydrogen, this solid releases H_2 over long periods of time (days or even weeks). The first contribution is the result of surface processes, while the second is linked to H_2 formation in the volume of the material, with the H_2 molecules, which are trapped in the crystal lattice, subsequently diffusing very slowly. Identifying the mechanisms involved in this system is, therefore, particularly interesting and important. To do this, we employed electron paramagnetic resonance, which can identify the paramagnetic species created on exposure to irradiation.

There are two types of mechanism for describing the surface and volume phenomena respectively. The first pathway involves the stabilization of the electrons on the surface of the portlandite, followed by surface reactions that promote the immediate release of H_2 into the gaseous atmosphere. The stabilization of electrons on surface sites implies that the samples with a greater specific surface area led to an immediate and larger production of H_2. The gradual reduction of these sites that enable the stabilization of electrons, however, results in a reduction in the effectiveness of this mechanism when the dose increases. Furthermore, the presence of trace metallic impurities, Cr^{3+}, in particular, inhibits this mechanism until these trace elements are depleted.

The second reaction pathway, called volume, involves H_2 being produced directly in the volume of the material. The H_2 produced can then migrate progressively from the volume to the surface to be released into the atmosphere. This mechanism is responsible for the delayed production of H_2. The special structure of portlandite enables the hydrogen atoms to move by jumping to Wyckoff sites, resulting in highly mobile $CaO^\bullet$ radicals. To begin with, this rapid movement

mechanism makes the $CaO^{\bullet}$ radicals react with each other, forming peroxides $CaO\text{-}OCa$ that cannot be detected by EPR. As the $H_{2(trapped)}$ accumulates in the structure, the $CaO^{\bullet}$ radicals can react with the trapped molecular hydrogen molecules, which destroys the molecules by forming hydrogen atoms. This recycling mechanism minimizes the amount of H_2 that could potentially be stored by the portlandite. The existence of other oxidizing species, such as $CaO_2^{\bullet}$ and $CaO_3^{\bullet}$, has also been demonstrated, and mechanisms that explain the appearance of these species have been suggested. Nonetheless, the role played by these species, in parallel with the production of radiolytic H_2, is not clear.

The use of an electron accelerator that enables irradiation at a very high dose rate of samples is not very representative of an operational context for storing radioactive waste. Irradiation in this context has a much lower dose rate, which almost certainly affects the values of the primary yields of the most reactive species and the resulting chemical equilibria. Furthermore, the portlandite examined in this study is a powdery material, unlike the portlandite found in real cementitious materials, which is present in the form of crystals several micrometers in size. It follows that further experiments are necessary to supplement the outcomes of this work. Lastly, the production of $H_{2(trapped)}$ in the volume of the material, its recycling and its transport from the volume to the surface are all phenomena that should be investigated in greater detail in anticipation of a coupled model that can explain the release of H_2 into the air.

Supporting Information

X-ray diffraction analysis; thermogravimetric analysis; power response curves for some defects in portlandite; comparison of the EPR spectra of U.P. and U.P.-L.S. portlandite; measurement of the rate constant of disappearance of $CaO^{\bullet}$ radicals; ^{17}O-enriched portlandite; calculation of the number of surface sites.

Acknowledgements

We would like to express our gratitude to EDF and CEA for their financial support. Our thanks go to Jorge Vieira for his help during the irradiation experiments with the ALIENOR linear accelerator. We would also like to thank the EMIR&A network; Audrey Courpron and Ozlem Oral for the EPR experiments; and Emilie Thory for the BET measurements.

References

(1) Rakhimova, N. Recent Advances in Alternative Cementitious Materials for Nuclear Waste Immobilization: A Review. *Sustainability* **2023**, *15*, 689. https://doi.org/10.3390/su15010689.

(2) Acher, L.; Chartier, D.; Dannoux-Papin, A.; Haas, J.; Courtial, M.; de Noirfontaine, M.-N.; Dunstetter, F.; Gorse-Pomonti, D.; Tusseau-Nenez, S. Radioactive Waste Conditioning : The Choice of the Cement Matrix versus Irradiation. In *37th Cement and Concrete Science Conference*, University College London, **2017**.

(3) Nakarai, K.; Niwase, K.; Miyamoto, M.; Sasaki, T. Low-Level Radioactive Waste Disposal in Japan and Role of Cementitious Materials. *J. Adv. Concr. Technol.* **2022**, *20*, 359–374. https://doi.org/10.3151/jact.20.359.

(4) Lothenbach, B.; Matschei, T.; Möschner, G.; Glasser, F. P. Thermodynamic Modelling of the Effect of Temperature on the Hydration and Porosity of Portland Cement. *Cem. Concr. Res.* **2008**, *38* (1), 1–18. https://doi.org/10.1016/j.cemconres.2007.08.017.

(5) Soin, A. V.; Catalan, L. J. J.; Kinrade, S. D. A Combined QXRD/TG Method to Quantify the Phase Composition of Hydrated Portland Cements. *Cem. Concr. Res.* **2013**, *48*, 17–24. https://doi.org/10.1016/j.cemconres.2013.02.007.

(6) Momma, K.; Izumi, F. VESTA 3 for Three-Dimensional Visualization of Crystal, Volumetric and Morphology Data. *J. Appl. Crystallogr.* **2011**, *44* (6), 1272–1276. https://doi.org/10.1107/S0021889811038970.

(7) LaVerne, J. A.; Tandon, L. H_2 and Cl_2 Production in the Radiolysis of Calcium and Magnesium Chlorides and Hydroxides. *J. Phys. Chem. A* **2005**, *109* (12), 2861–2865. https://doi.org/10.1021/jp044166o.

(8) Herin, T.; Charpentier, T.; Bouniol, P.; Le Caër, S. Behavior of Portlandite upon Exposure to Ionizing Radiation: Evidence of Delayed H_2 Production. *J. Phys. Chem. C* **2023**, *127* (41), 20245–20254. https://doi.org/10.1021/acs.jpcc.3c05012.

(9) McCluskey, M. D.; Jokela, S. J. Defects in ZnO. *J. Appl. Phys.* **2009**, *106*, 071101. https://doi.org/10.1063/1.3216464.

(10) Wang, J. X.; Lunsford, J. H. Characterization of [Li^+O^-] Centers in Lithium-Doped MgO Catalysts. *J. Phys. Chem.* **1986**, *90* (22), 5883–5887. https://doi.org/10.1021/j100280a084.

(11) Henderson, B.; Tohver, H. T. EPR Studies of Impurities in Electron-Irradiated CaO. *Phys.stat.sol (b)* **1972**, *51* (2), 761–768. https://doi.org/10.1002/pssb.2220510235.

(12) Abraham, M. M.; Chen, Y. V- and V° Centers in CaO Single Crystal*. *Solid State Commun.* **1975**, *16*, 1209–1213.

(13) Barsova, L. I.; Yurik, T. K.; Spitsyn, V. I. Radiation Centers in Alkaline-Earth Hydroxides. *Inorg. Chem.* **1986**, *35* (5), 879–883. https://doi.org/https://doi.org/10.1007/BF00955340.

(14) Yurik, T. K.; Ionova, G. V; Barsova, L. I.; Spitsyn, V. I. ESR Investigation of Hydrogen Atoms Stabilized in γ -Irradiated Alkaline Earth Hydroxides. In *Radiation Effects and Defects in Solid*; 1988; pp 87–98. https://doi.org/10.1080/00337578808013731.

(15) L.I.Barsova. Atomic Hydrogen in Gamma-Irradiated Hydroxides of Alkaline-Earth Elements. *URSS Chem Bull* **1982**, *31*, 672–677. https://doi.org/https://doi.org/10.1007/BF00949995.

(16) Mialocq, J. C.; Hickel, B.; Baldacchino, G.; Juillard, M. The Radiolysis Project of CEA.Pdf. *J. Chim. Phys.* **1999**, *96* (1), 35–53. https://doi.org/https://doi.org/10.1051/jcp:1999108.

(17) Fricke, H.; Hart, J. E., Editors Attix, F.H. and Roesch, W.C. in *Radiation Dosimetry, 2nd Ed*; Academic Press, New York, **1966**, 167-239.

(18) Berger, M. J.; Coursey, J. S.; Zucker, M. A.; Chang, J. NIST Standard Reference Database 124. 2017. https://doi.org/https://dx.doi.org/10.18434/T4NC7.

(19) Yordanov, N. D. Quantitative EPR Spectrometry - "State of the Art." *Appl. Magn.Reson* **1994**, *6*, 241–257.

(20) Regulla, D. F.; Deffner, U. Dosimetry by ESR Spectroscopy of Alanine. *Int. J. Radiat. Appl.* **1982**, *33*, 1101–1114.

(21) Van Laere, K.; Buysse, J.; Berkens, P. Alanine in High-Dose Dosimetry Spectrophotometric and Electrochemical Readout Procedures Compared with ESR. *Int. J. Radiat. Appl. lnstrum* **1989**, *40* (10–12), 885–895.

(22) Panta, P. P.; Strzelczak-Burlinska, G.; Tomasinski, Z. ESR/L-Alanine System as a Proposed Standard Dosimeter for Electron-Beam Irradiations. *Int. J. Radiat. Appl. lnstrum* **1989**, *40* (10), 971–975.
(23) Nakagawa, K.; Eaton, S. S.; Eaton, G. R. Electron Spin Relaxation Times of Irradiated Alanine. *Appl. Radiat. Isot.* **1993**, *44* (1–2), 73–76.
(24) Gottschall, W. C.; Tolbert, B. M. The Radiation Chemistry of Anhydrous Solid State Glycine, Alanine, and Glycine Salts. *Radiat. Chem.* **1968**, *26*, 374–383.
(25) Stoll, S.; Schweiger, A. EasySpin , a Comprehensive Software Package for Spectral Simulation and Analysis in EPR. *J. Magn. Reson.* **2006**, *178*, 42–55. https://doi.org/10.1016/j.jmr.2005.08.013.
(26) Stoll, S. CW-EPR Spectral Simulations : Solid State. *Methods Enzymol.* **2015**, *563*, 121–142.
(27) Holuj, F.; Wieczorek, J. V Centers in $Ca(OH)_2$, and $Ca(OD)_2$. *J. Magn. Reson.* **1977**, *25*, 211–217.
(28) Ferrari, A. M.; Pacchioni, G.; Inorgánica, C.; Milano, U. Electronic Structure of F and V Centers the MgO Surface. **1995**, No. 100, 17010–17018.
(29) Alfaro Cruz, M. R.; Luévano-Hipolito, E.; Garza-Hernandez, R.; Torres-Martinez, L. M. MgO and Mg $(OH)_2$ Thin Films Prepared by the SILAR Method and Their CO_2 Photocatalytic Performance. *J Mater Sci* **2022**, *57*, 18739–18753. https://doi.org/10.1007/s10853-022-07837-x.
(30) Kantorovich, L. N.; Holender, J. M.; Gillan, M. J. The Energetics and Electronic Structure of Defective and Irregular Surfaces on MgO. *Surf. Sci.* **1995**, *343*, 221–239.
(31) Sousa, C.; Pacchioni, G.; Illas, F. Ab Initio Study of the Optical Transitions of F Centers at Low-Coordinated Sites of the MgO Surface. *Surf. Sci.* **1999**, *429*, 217–228.
(32) Cordischi, D.; Indovina, V.; Occhiuzzi, M. Electron Spin Resonance Studies of the Formation and Thermal Stability of Oxygen Radicals on CaO and Some Other Oxides. *J. Chem. Soc. Faraday Trans. 1 Phys. Chem. Condens. Phases* **1978**, *74*, 883–892. https://doi.org/10.1039/F19787400883.
(33) Wong, N. B.; Lunsford, J. H. EPR Study of O_3^- on Magnesium Oxide. *J. Chem. Phys.* **1972**, *56*, 2664–2667. https://doi.org/10.1063/1.1677594.
(34) Chiesa, M.; Paganini, M. C.; Giamello, E.; Murphy, D. M. Surface Color Centers on Calcium Oxide : An Electron Paramagnetic Resonance Investigation. *Langmuir* **1997**, *13* (19), 5306–5315.
(35) Mohl, W.; Boer, E. De; Doorslaer, S. Van; Callens, F.; Sothe, H.; Luty, F. Properties of Electron-Irradiation-Produced O_2^- in $Ca(OH)_2$. *J. Phys. Chem. C Solid State Phys* **1980**, *13*, 5481.
(36) Debuyst, R.; Bidiamambu, M.; Dejehet, F. An EPR Study of γ- and α-Irradiated Synthetic Powdered Calcite Labelled with ^{13}C. *Int. J. Radiat. Appl. Instrumentation. Part* **1991**, *18* (1–2), 193–201. https://doi.org/10.1016/1359-0189(91)90113-V.
(37) Wencka, M.; Lijewski, S.; Hoffmann, S. K. Dynamics of CO_2^- Radiation Defects in Natural Calcite Studied by ESR, Electron Spin Echo and Electron Spin Relaxation. *J. Phys. Condens. Matter* **2008**, *20*, 255237–255247. https://doi.org/10.1088/0953-8984/20/25/255237.
(38) Halliburton, L. E.; Giles, N. C.; Garces, N. Y.; Luo, M.; Xu, C. Production of Native Donors in ZnO by Annealing at High Temperature in Zn Vapor. *Appl. Phys. Lett.* **2005**, *87*, 172108–172111. https://doi.org/http://dx.doi.org/10.1063/1.2117630.
(39) Gonzalez, C.; Galland, D.; Herve, A. Interactions Hyperfines Du Centre F+ Dans ZnO. *Phys.stat.sol (b)* **1975**, *72*, 309–320.
(40) Smith, J. M.; Vehse, W. E. ESR of Electron Irradiated ZnO Confirmation of the F+ Center. *Phys. Lett.* **1970**, *31A* (3), 3–4.
(41) Tench, A. J.; Lawson, T. The Formation of O^- and O_3^- Adsorbed on an Oxide Surface. *Chem. Phys. Lett.* **1970**, *7* (4), 459–460. https://doi.org/10.1016/0009-2614(70)80335-9.
(42) Kaddissy, J. A.; Esnouf, S.; Durand, D.; Saffre, D.; Foy, E.; Renault, J.-P. Radiolytic Events in Nanostructured Aluminum Hydroxides. *J. Phys. Chem. C* **2017**, *121* (11), 6365–6373. https://doi.org/10.1021/acs.jpcc.6b13104.
(43) Born, G.; Hofstaetter, A.; Scharmann, A. EPR of Pb^{3+} in ZnO. *Z.Physik* **1970**, *240*, 163–167.
(44) Dongming, Z.; Kittilstved, K. R. Control over Fe^{3+} Speciation in Colloidal ZnO Nanocrystals. *J. Mater. Chem. C* **2015**, *3*, 4352–4358. https://doi.org/10.1039/C5TC00470E.
(45) Chakradhar, R. P. S.; Sivaramaiah, G.; Lakshmana RaO, J.; Gopal, N. O. Fe^{3+} Ions in Alkali

Lead Tetraborate Glasses — an Electron Paramagnetic Resonance and Optical Study. *Spectrochim. Acta Part A* **2005**, *62*, 51–57. https://doi.org/10.1016/j.saa.2004.12.004.

(46) Ardelean, I.; Peteanu, M.; Simon, V.; Bob, C. EPR and Magnetic Susceptibility Studies of Cr_2O_3 – Bi_2O_3 – GeO_2 Glasses. *J. Mater. Sci.* **1998**, *33*, 357–362.

(47) Sreekanth Chakradhar, R. P.; Lakshmana Rao, J.; Sivaramaiah, G.; Gopal, N. O. Chromium Ions in Alkali Lead Borotellurite Glasses – An EPR and Optical Study. *Phys.stat.sol (b)* **2005**, *2929* (14), 2919–2929. https://doi.org/10.1002/pssb.200540100.

(48) Pishtshev, A.; Karazhanov, S. Z.; Klopov, M. Excitons in $Mg(OH)_2$ and $Ca(OH)_2$ from Ab Initio Calculations. *Solid State Commun.* **2014**, *193*, 11–15. https://doi.org/10.1016/j.ssc.2014.05.019.

(49) Thomas, J. K. Physical Aspects of Radiation-Induced Processes on SiO_2, γ-Al_2O_3, Zeolites, and Clays. *Chem. Rev.* **2005**, *105* (5), 1683-1734.

(50) Jones, B. M.; Aleksandrov, A. B.; Zhang, X.; Rosso, K. M.; LaVerne, J. A.; Orlando, T. M. Electron-Stimulated Formation and Release of Molecular Hydrogen and Oxygen from Boehmite Nanoplatelet Films. *J. Phys. Chem. C* **2022**, *126* (5), 2542–2547. https://doi.org/10.1021/acs.jpcc.1c09673.

(51) Dupuis, R.; Dolado, J. S.; Benoit, M.; Surga, J.; Ayuela, A. Quantum Nuclear Dynamics of Protons within Layered Hydroxides at High Pressure. *Sci. Rep.* **2017**, *7*, 4842–4849. https://doi.org/10.1038/s41598-017-04080-2.

(52) Raugei, S.; Luigi Silvestrelli, P.; Parrinello, M. Pressure-Induced Frustration and Disorder in $Mg(OH)_2$ and $Ca(OH)_2$. *Phys. Rev. Lett.* **1999**, *83* (11), 2262–2265. https://doi.org/10.1103/PhysRevLett.83.2222.